Research Article Vol. 29, No. 2 / 18 January 2021 / Optics Express 1244

Optics EXPRESS

Non-Planckian infrared emission from GaAs devices with electrons and lattice out-of-thermal-equilibrium

YUEXIN ZOU,[1] HONG PAN,[1] SHENYANG HUANG,[1] PINGPING CHEN,[2] HUGEN YAN,[1] AND ZHENGHUA AN[1,3,4,5,*]

[1] *Laboratory of Advanced Materials, State Key Laboratory of Surface Physics, and Department of Physics, Fudan University, Shanghai 200438, China*
[2] *National Laboratory for Infrared Physics, Shanghai Institute of Technical Physics, Chinese Academy of Sciences, Shanghai 200083, China*
[3] *Institute of Nanoelectronic Devices and Quantum Computing, Fudan University, Shanghai 200438, China*
[4] *Shanghai Qi Zhi Institute, 41th Floor, AI Tower, No. 701 Yunjin Road, Xuhui District, Shanghai 200232, China*
[5] *State Key Laboratory of Applied Optics, Changchun Institute of Optics, Fine Mechanics and Physics, Chinese Academy of Sciences, Changchun 130033, China*
[*] *anzhenghua@fudan.edu.cn*

Abstract: With the downscaled device size, electrons in semiconductor electronics are often electrically driven out-of-thermal-equilibrium with hosting lattices for their functionalities. The thereby electrothermal Joule heating to the lattices can be visualized directly by the noncontact infrared radiation thermometry with the hypothetic Planck distribution at a single characteristic temperature. We report here that the infrared emission spectrum from electrically biased GaAs devices deviates obviously from Planck distribution, due to the additional contribution from non-equilibrium hot electrons whose effective temperature reaches much higher than that of the lattice ($T_e > T_l$). The evanescent infrared emission from these hot electrons is out-coupled by a near-field metamaterial grating and is hence made significant to the total far-field emission spectrum. Resonant emission peak has also been observed when the electron hotspots are managed to overlap spatially with the optical hotspots at the grating resonance. Our work opens a new direction to study nonequilibrium dynamics with (non-Planckian) infrared emission spectroscopy and provides important implications into the microscopic energy dissipation and heat management in nanoelectronics.

1. Introduction

Planck's law of blackbody radiation historically played a milestone role in the development of quantum mechanics physics and nowadays has penetrated into a broad range of applications such as cosmology, astronomy, thermal imaging, spectroscopy, security, biology, clinics, etc. [1]. According to Planck's law, the spectral radiance of a blackbody for frequency ν at a single absolute temperature T can be written as,

$$I_{bb}(\nu, T) = \frac{2h\nu^3}{c^2} \frac{1}{e^{h\nu/k_B T} - 1} \tag{1}$$

where k_B is the Boltzmann constant, h is the Planck constant, and c is the speed of light. Planck's formula, however, applies only in far field with distance being much longer than the thermal length ($d >> \lambda_{th}$) and also for thermal equilibrium objects with uniform temperature distributions (T). Recent studies have unambiguously demonstrated super-Planckian radiation in the thermal near-field ($d < \lambda_{th}$) [2–4], which can be utilized to boost the radiative energy transfer [5–7], non-contact cooling [8], thermophotovoltaic cells [9] etc.

#415232 https://doi.org/10.1364/OE.415232
Journal © 2021 Received 17 Nov 2020; revised 15 Dec 2020; accepted 20 Dec 2020; published 6 Jan 2021

On the other hand, very few works so far have devoted to the emission properties of thermal *non-equilibrium* objects, despite the fact that non-equilibrium charge transport prevails in modern semiconductor nanoelectronics [10–12]. In the miniatured transistors, electrons are accelerated by external bias and thereby thermalized to a very high effective temperature, T_e, on the order of $10^3 \sim 10^4$K ($T_e >> T_l$) [13], due to typically faster electron-electron scattering than electron-phonon scattering. The subsequent energy relaxation of these hot electrons causes substantial Joule heating to lattices, thereby leads to huge burden to the cooling efficiency of the high-integration chips and bottlenecks the further improvement of the device performance [10]. Our previous work probed the near-field emission of hot electrons at a single wavelength (~14.1µm) in a GaAs nanoconstricted channel and evaluated that the effective electron temperature reaches $\mathrm{T_e}$~2000K in a room temperature current-carrying device ($\mathrm{T_l}$~300K) [14]. The spatial profile of the observed single wavelength emission pattern revealed the remarkable nonlocality of energy relaxation of the transporting hot electrons across a nanoconstricted channel. However, the spectral studies of infrared emission from these non-equilibrium systems remain unexplored, despite of their abundant energy dynamics information behind [15].

In this work, we report the experimental results of infrared emission spectrum from a non-equilibrium GaAs system. Electrons inside the devices are electrically biased and driven to be out-of-thermal-equilibrium with GaAs lattices. The measured infrared spectrum distinguishes from the predicted black-body or gray-body radiation at a single sample temperature and implies the non-equilibrium radiation feature of the current-carrying devices. Our work establishes a general approach to study dynamics in nonequilibrium objects with infrared emission spectroscopy and provides important hints into the microscopic heat management in semiconductor nanodevices.

2. Method and results

The devices were fabricated on GaAs wafers with a 35nm-thick and *n*-type doped GaAs quantum well (QW) grown on semi-insulating GaAs substrate and subsequently capped by a 13-nm top AlGaAs insulating layer, same as in Ref. [14]. The electron density in the QW and the electron mobility at room temperature are measured to be $\mathrm{n_{2D}} = 1.10 \times 10^{17}$ $\mathrm{m^{-2}}$ (or $\mathrm{n_{3D}} = 3.3 \times 10^{24}$ $\mathrm{m^{-3}}$) and $\mu = 0.167$ $\mathrm{m^2/Vs}$. Four-terminal devices were fabricated by standard lithography, as shown in Fig. 1(a). Cross-shaped mesa structures were made by wet etching with annealed Ni/AuGe/Au (10nm/100nm/100nm) pads as Ohmic contacts. The center region (100µm×100µm) of the cross-shaped channel were finally covered by a two-dimensional metamaterial grating (5nm Cr/60nm Au) via electron-beam lithography and lift-off processes. Figure 1(b) depicts the scanning electron microscopic (SEM) images of the grating pattern. Each rectangle unit cell has a side-length of 2µm (perpendicular to Au rod) and the other side length of 4.5µm (parallel with Au rod). The length and width of Au rod are fixed to be L=2.25µm and w=0.25µm in this work. By applying electrical bias to a pair of electrodes (left and right electrodes, or top and bottom electrodes), the center region with metamaterial grating was electrothermally heated and the thereby emitted radiation was collected by a Bruker Hyperion 1000 microscope and analyzed spectroscopically by a Fourier Transform Infrared Spectroscope (FTIR) Vertex 70. An aperture was employed in the light path to ensure the detected region being the center 100µm×100µm area. To avoid the influence of background, the devices were excited by periodic electric pulses and the emission signal was measured by a cooled mercury cadmium telluride (MCT) detector, demodulated with a lock-in amplifier, and then recorded in the step-scan mode of the FTIR system. Figure 1(c) schematically shows the measurement setup. To take account of both optical path efficiency and electronic amplification coefficient in this setup, a black-painted ceramic sample which can be assumed to be close to ideal blackbody was used and the temperature dependent measurement in the range of 300K~500K was performed to calibrate the whole system. The measured spectra for all samples can therefore be normalized and directly compared with theoretical calculations.

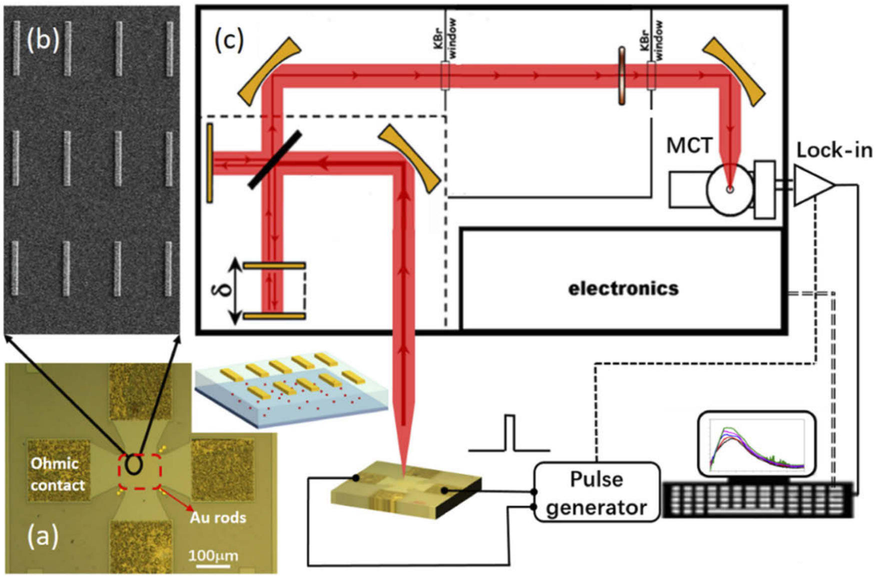

Fig. 1. (a) Optical microscopic image of the four-terminal devices fabricated on GaAs quantum well wafer. Right inset is the schematic structure of the device infrared-emitting region with metal metamaterial grating (yellow) and hot electrons (red). (b) Scanning electron microscopic (SEM) image of the metamaterial grating with periodic Au-rod structure (L=2.25μm and w=0.25μm). The unit cell size is 2μm × 4.5μm. (c) Experimental setup for the emission spectrum measurement using an FTIR spectrometer working at step-scan mode. The sample is biased with a pulse generator.

Before applying the electric pulse excitations, control experiments were carried out by directly heating the entire samples with a heating stage, which therefore led to an equilibrium condition with T_e=T_l (≡T_s). The measured spectra were displayed in Fig. 2(a) as lines with dots for different temperatures (T_s=60°C, 90°C, 150°C). For comparison, expected emission spectra in the same frequency range are also calculated based on the grey-body assumption, i.e., $I_{gb}(\nu, T) = \epsilon \times I_{bb}(\nu, T)$, where ϵ is the emissivity. Dashed curves show the calculated emission spectra of samples with different temperatures T_s=60°C, 90°C, 150°C respectively, and the temperature independent emissivity for the samples is obtained through independent calibration measurement following the standard procedure in Ref. [16]. It can be seen that reasonable agreement can be reached between the experimental and calculated data, implying the validity of Planck distribution for this condition and hence the grey-body approximation. Solid curves in Fig. 2(b) shows the emission spectra measured with pulsed bias (at 517Hz, with 50% duration of $2V_b$ and the other 50% duration, 0V) between left and right electrodes of the sample (the flowing current is perpendicular to Au nanorods). With increasing the pulse amplitude (V_b), the emission intensity increases rapidly, suggesting that the sample temperature increases. It is, however, found that these spectra cannot be reproduced consistently by simulation with a single temperature (T_s). Dashed curves in Fig. 2(b) represent the simulated emission for T_s=100°C~350°C. Remarkable difference can be seen especially for high temperatures. For instance, for the spectra taken at $V_b = 40$V, the calculation with $T_s = 300$°C overestimates the emission intensity in the high frequency region (>1500cm^{-1}) while underestimates in low frequency region. The large discrepancy implies the invalidity of thermal-equilibrium assumption for the electrothermal heating condition in our samples. Although the direct measurement of T_s under electrical bias will be informative, non-contact radiative thermometric method does not work because of the non-Planckian characteristic while the direct contact-type thermometer (such as thermocouple) remains to be technologically challenging so far.

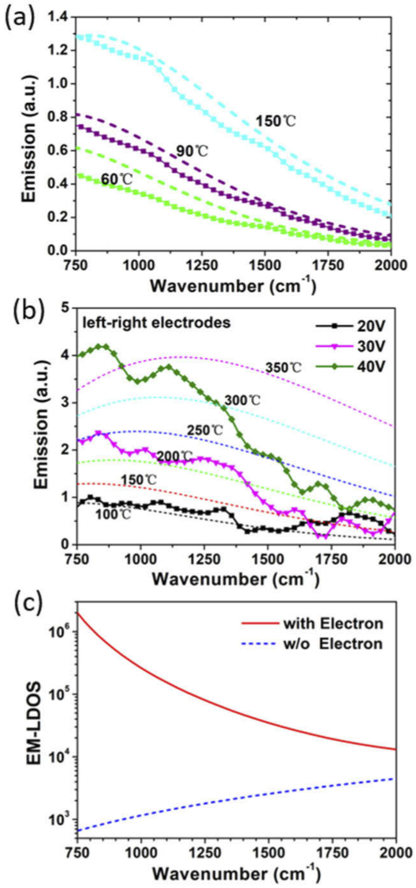

Fig. 2. (a) Emission spectra (lines with dots) taken with the sample being uniformly heated to different temperatures (T_e=T_l=60°C, 90°C, 150°C), using a controllable electrothermal stage. Dashed lines are calculated data from Planck's law and show reasonable agreement with experiments. (b) Emissions with different pulses applied to left-right electrodes (lines with dots). Calculation from Planck's law (dashed lines) show obvious deviation with experimental curves. (c) Electromagnetic local density of states (EM-LDOS) for the GaAs crystal structure with (solid red) and without (dashed blue) conducting electrons.

To explain the above discrepancy (Fig. 2(b)), we recall that the emission from hot electrons can be characterized by the electromagnetic local density of states (EM-LDOS), which decays rapidly with increasing the height from the sample surface [17,18]. In Ref. [14], a metal tip was used to scatter this evanescent emission into far-field for detection and, here, the metamaterial grating plays a similar role but functions over much larger area so that the significant portion of the electron emission can be out-coupled and contribute to the measured spectra. Figure 2(c) displays the EM-LDOS calculated for GaAs sample with conducting electrons (solid red), using a Drude model for conducting electrons ($\varepsilon = \varepsilon_{GaAs} + \frac{{\omega_p}^2}{\omega(\omega+i\cdot\gamma)}$, in which $\varepsilon_{GaAs} = 12.9$, $\omega_p = 4.0 \times 10^{14} rad/s$ and $\gamma = 1.6 \times 10^{13} rad/s$) [19]. These parameters are evaluated according to the electron density in the measured real samples so that the result is close to the real situation. For comparison, the EM-LDOS for same GaAs material but without conducting electrons was also calculated by omitting the Drude term (i.e., $\varepsilon = \varepsilon_{GaAs} = 12.9$) and shown as dashed blue curve in Fig. 2(c). It can be seen that GaAs without conducting electrons exhibits much lower EM-LDOS, particularly in the low-frequency spectral range. The EM-DOS of electrons gives larger contribution at lower frequency range and we can therefore expect that inclusion of hot electron contribution into the total emission spectra provides reasonable explanation to the observed non-Planckian emission.

Next, we switched the electrical bias to top-bottom electrode pair (instead of left-right pair in Fig. 2), generating electrical current being parallel to Au nanorods. In this case, the metamaterial grating plays the same role as in Fig. 2 extracting the near-field emission from hot electrons to the far-field. In addition, note that each Au nanorod keeps to be equipotential even when a large bias is applied, and therefore functions as a surface gate to modulate the underlying electric field distributions in QW layer. To provide semiquantitative analysis, finite-element numerical simulation was performed by using a commercial multiphysics software. In this simulation, the conducting layer (35nm-thick GaAs quantum well layer) was separated into two physical sheets representing, respectively, the electron and the lattice subsystems, as schematically shown in Fig. 3(a). The heat transferred from electron to lattice is characterized by the temperature difference ($T_e - T_l$) times the effective interface thermal resistance $h_{\mathrm{e-ph}}$ which can be written as $h_{\mathrm{e-ph}} = \tau_{\mathrm{e-ph}}/C_{\mathrm{e}}$, where $\tau_{\mathrm{e-ph}}$ is the electron-phonon scattering time and C_{e}, the electron specific heat per unit area. The electric field and the heat arising from the electrical current can be simulated according to Ohm's law and Joule's law respectively in the electromagnetics module and then the heat is dissipated through Fourier's law of heat conduction in the heat transfer module. Eventually the temperature distributions depending on the electrical bias can be obtained through this convenient method, see Ref. [20] for more details. Figure 3(c) displays the simulated electric field distribution in three-unit-cell with the finite-element method and it can be seen that the field maxima appears nearby the two ends of the nanorods. As a result, substantially nonuniform distributions of the electron temperatures are produced with electron hotspots located nearby the two ends of the nanorods. Fig ure 3(d) shows the simulated results of the two-dimensional temperature distribution using the method established in Ref. [20]. The peak T_e at hotspots reaches ~1400K, which agrees reasonably with previous work [21]. Figure 3(g) displays the measured spectra (solid curves) for different bias amplitudes, which cannot be reproduced by simulations with single temperatures (dashed lines). Similar to Fig. 2(b), the emission intensity increases with the electrical bias. On the other hand, however, an additional peak shows up at ~1200cm^{-1}. This frequency agrees reasonably with the simulated resonance (~1200cm^{-1}) of the metamaterial grating with y-polarized excitation. The observed emission spectral peak can therefore be attributed to the resonant enhancement of the hot electron infrared emission. Figure 3(e) demonstrates the spatial distribution of the *optical* electric field at resonance. It can be seen that the hotspot of the optical field matches that of the electron temperature much better than in Fig. 2. Figure 3(f) shows the line-plots along y-direction for optical electric field (blue dashed curve) and electron temperature (red solid curve) and the improved overlapping of the hotspot region becomes obvious. It is worth mentioning that, in Fig. 2, the electric current is perpendicular to the nanorods and the rather narrow width of the nanorods gives rise to a limited influence to the potential gradient and, as a result, the electron temperature has a quite uniform distribution. In this condition, the x-polarized field plays a more dominant role which has a much higher resonant frequency (~2700cm^{-1}), well beyond the studied spectral range. Therefore, the measured spectra in Fig. 2 arise from nonresonant scattering and extraction of the hot electron emission by metamaterial grating. In contrast, in Fig. 3, resonant enhancement of the hot electron contribution to the emission spectrum arises due to the improved overlapping between electron temperature distributions and the resonant optical electric field distributions. The remarkable contribution of this resonant contribution can be further elucidated by the bias-dependent emission, as displayed in Fig. 3(h). Apparently superlinear behavior can be identified in the range of large input power, indicating that certain enhancement mechanism such as Purcell-effect is involved [22–24]. The resonant enhancement provides an interesting means to tune the infrared emission from hot electrons through, e.g., the grating periodicity. Despite that more quantitative studies are necessary in future, our work here present unambiguously the effectiveness of metamaterial grating in coupling electron heat out of the lattice environment.

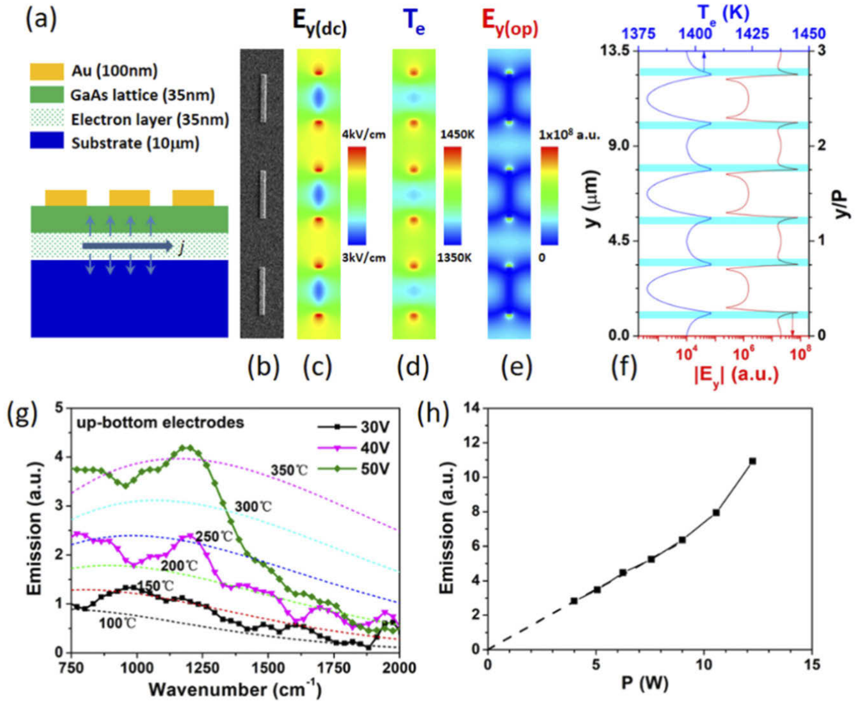

Fig. 3. (a) Schematic structure to simulate the nonequilibrium heat transport. The electric current *j* in the electron layer (dotted green) generates heat through Joule effect and part of the heat thereby is transferred to the lattice (both upper green and lower blue) through electron-phonon interaction, indicated by vertical arrows. (b-e) The SEM (b), electric field (c), effective electron temperature (d) when the device is biased between top-bottom electrodes, and optical electric field at the grating resonant frequency of 1200cm^{-1} (e). In (c-e), the red color indicates a large electric-field or higher temperature while blue, smaller field or lower temperature. All color bars are in linear scale. (f) Line profiles of T_e and optical electric field taken from (d) and (e). Overlapping between the electron hotspot and grating optical-field hotspot is apparent as indicated by the shadowed region. (g) Emissions with different pulses applied to top-bottom electrodes (lines with dots). Calculation from Planck's law is also shown as dashed line. Additional peak shows up at ~1200cm^{-1} when the bias voltage increases. (h) Dependence of the emission intensity on the input electric power, showing super-linear behavior at large biases.

3. Conclusion

In summary, we report here the first emission spectral measurements on hot-electron semiconductor devices with $T_e > T_l$ and the observed non-Planckian emission can be ascribed to the evanescent hot electron emission being out-coupled by metamaterial grating. Both nonresonant and resonant extraction of hot electron emission by the metamaterial grating can be identified. Our work opens a new direction to study nonequilibrium dynamics with infrared emission spectroscopy and provides new important hints to the microscopic heat management in nanoelectronics.

Funding. Shanghai Science and Technology Committee (18JC1420402, 18JC1410300, 20JC1414700, 20DZ1100604); National Natural Science Foundation of China (12027805, 11991060, 11674070, 11634012); National Key Research Program of China (2016YFA0302000).

Acknowledgments. Part of the device fabrication was performed at the Fudan Nanofabrication Laboratory.

Disclosures. The authors declare no conflicts of interest.

References

1. A. Rogalski, “Infrared detectors: Status and trends,” Progress in Quantum Electronics **27**(2-3), 59–210 (2003).
2. J. C. Cuevas, “Thermal radiation from subwavelength objects and the violation of Planck’s law,” Nat. Commun. **10**(1), 3342–3344 (2019).
3. J. Yang, W. Du, Y. Su, Y. Fu, S. Gong, S. He, and Y. Ma, “Observing of the super-Planckian near-field thermal radiation between graphene sheets,” Nat. Commun. **9**(1), 1–10 (2018).
4. D. Thompson, L. Zhu, R. Mittapally, S. Sadat, Z. Xing, P. McArdle, M. M. Qazilbash, P. Reddy, and E. Meyhofer, “Hundred-fold enhancement in far-field radiative heat transfer over the blackbody limit,” Nature **561**(7722), 216–221 (2018).
5. E. Rousseau, A. Siria, G. Jourdan, S. Volz, F. Comin, J. Chevrier, and J.-J. Greffet, “Radiative heat transfer at the nanoscale,” Nat. Photonics **3**(9), 514–517 (2009).
6. K. Kim, B. Song, V. Fernández-Hurtado, W. Lee, W. Jeong, L. Cui, D. Thompson, J. Feist, M. T. H. Reid, F. J. García-Vidal, J. C. Cuevas, E. Meyhofer, and P. Reddy, “Radiative heat transfer in the extreme near field,” Nature **528**(7582), 387–391 (2015).
7. L. Worbes, D. Hellmann, and A. Kittel, “Enhanced Near-Field Heat Flow of a Monolayer Dielectric Island,” Phys. Rev. Lett. **110**(13), 134302 (2013).
8. L. Zhu, A. Fiorino, D. Thompson, R. Mittapally, E. Meyhofer, and P. Reddy, “Near-field photonic cooling through control of the chemical potential of photons,” Nature **566**(7743), 239–244 (2019).
9. D. Fan, T. Burger, S. McSherry, B. Lee, A. Lenert, and S. R. Forrest, “Near-perfect photon utilization in an air-bridge thermophotovoltaic cell,” Nature **586**(7828), 237–241 (2020).
10. M. M. Waldrop, “More than Moore,” Nature **530**(7589), 144–147 (2016).
11. L.-F. Mao, “Energy relaxation of electrons impacts on channel quantization in nano-MOSFETs,” Appl. Phys. A **117**(4), 1835–1840 (2014).
12. E. Pop, “Energy dissipation and transport in nanoscale devices,” Nano Res. **3**(3), 147–169 (2010).
13. H. Rao and G. Bosman, “Hot-electron induced defect generation in AlGaN/GaN high electron mobility transistors,” Solid-State Electronics **79**, 11–13 (2013).
14. Q. Weng, S. Komiyama, L. Yang, Z. An, P. Chen, S.-A. Biehs, Y. Kajihara, and W. Lu, “"Imaging of nonlocal hot-electron energy dissipation via shot noise,” Science **360**(6390), 775–778 (2018).
15. G. Cabra, M. D. Ventra, and M. Galperin, “Local-noise spectroscopy for nonequilibrium systems,” Phys. Rev. B **98**(23), 235432 (2018).
16. J. Mink, “Infrared Emission Spectroscopy,” in *Handbook of Vibrational Spectroscopy* (Wiley, 2006), Vol. 2.
17. K. Joulain, R. Carminati, J.-P. Mulet, and J.-J. Greffet, “Definition and measurement of the local density of electromagnetic states close to an interface,” Phys. Rev. B **68**(24), 245405 (2003).
18. A. C. Jones, B. T. O’Callahan, H. U. Yang, and M. B. Raschke, “The thermal near-field: Coherence, spectroscopy,heat-transfer, and optical forces,” Prog. Surf. Sci. **88**(4), 349–392 (2013).
19. P. G. Huggard, J. A. Cluff, G. P. Moore, C. J. Shaw, S. R. Andrews, S. R. Keiding, E. H. Linfield, and D. A. Ritchie, “Drude conductivity of highly doped GaAs at terahertz frequencies,” J. Appl. Phys. **87**(5), 2382–2385 (2000).
20. L. Yang, R. J. Qian, Z. H. An, S. Komiyama, and W. Lu, “Simulation of temperature profile for the electron- and the lattice-systems in laterally structured layered conductors,” Europhys. Lett. **128**(1), 17001 (2019).
21. V. Aninkevičius, V. Bareikis, R. Katilius, J. Liberis, I. Matulionienė, A. Matulionis, P. Sakalas, and R. Šaltis, “Γ-X intervalley-scattering time constant for GaAs estimated from hot-electron noise spectroscopy data,” Phys. Rev. B **53**(11), 6893–6895 (1996).
22. J. Shang, C. Cong, Z. Wang, N. Peimyoo, L. Wu, C. Zou, Y. Chen, X. Yu Chin, J. Wang, C. Soci, W. Huang, and T. Yu, “Room-temperature 2D semiconductor activated vertical-cavity surface-emitting lasers,” Nat. Commun. **8**(1), 543 (2017).
23. R.-J. Shiue, Y. Gao, C. Tan, C. Peng, J. Zheng, D. K. Efetov, Y. D. Kim, J. Hone, and D. Englund, “Thermal radiation control from hot graphene electrons coupled to a photonic crystal nanocavity,” Nat. Commun. **10**(1), 109 (2019).
24. T. Inoue, M. De Zoysa, T. Asano, and S. Noda, “Realization of dynamic thermal emission control,” Nat. Mater. **13**(10), 928–931 (2014).